JOURNAL OF APPLIED ELECTROCHEMISTRY **16** (1986) 345–356

Electrochemical machining of refractory materials

CORINNE A. COUGHANOWR,* BERNARD A. DISSAUX, ROLF H. MULLER, CHARLES W. TOBIAS

Lawrence Berkeley Laboratory, Materials and Molecular Research Division and Department of Chemical Engineering, University of California, Berkeley, CA 94720, USA

Received 28 September 1984; revised 8 May 1985

The feasibility of the electrochemical machining (ECM) of pure TiC, ZrC, TiB_2 and ZrB_2 has been established. In addition, the ECM behaviour of a cemented TiC/10% Ni composite has been investigated and compared to that of its components, TiC and nickel. ECM was carried out in 2 M KNO_3 and in 3 M NaCl at applied voltages of 10–31 V and current densities of 15–115 A cm^{-2}. Post-ECM surface studies on the TiC/Ni composite showed preferential dissolution of the TiC phase during machining.

Nomenclature

E_0	thermodynamic equilibrium potential (V)
F	Faraday's constant (96 500 Coul mol^{-1})
$\dot{x}$	toolpiece feed rate (cm s^{-1} or mm min^{-1})
I	current (A)
i	current density (A cm^{-2})
k	electrolyte conductivity (Ω^{-1} cm^{-1})
l	interelectrode gap (mm)
$\dot{m}$	mass removal rate (g s^{-1} or g min^{-1})
M	formula weight (g mol^{-1})
Q	electrolyte flow rate (l min^{-1})
t	electrolyte temperature (° C)
V	applied voltage (V)
V_{IR}	ohmic drop through electrolyte (V)
z	apparent valence of dissolution (eq mol^{-1})
η_i	overvoltages (V)
ϱ	density of refractory materials (g cm^{-3})

1. Introduction

Electrochemical machining (ECM) is a process of metal removal by high-rate anodic dissolution. The material to be machined must be an electronic conductor; its ECM behaviour is determined by its electrochemical nature and not by its hardness. Thus, for shaping very hard materials ECM is an attractive alternative to conventional mechanical methods of machining; cutting time and toolpiece wear are much lower in ECM. Because of the limited ability to predict quantitatively the workpiece shape and surface finish from system variables, applications of this technique have advanced relatively slowly.

The transition metal carbides and borides have potential for widespread use in the aerospace industry because of their very high melting points and extreme hardness [1, 2]. The carbides and borides of titanium and zirconium were selected for investigation in this laboratory. Current uses for TiC which require shaping include tools for metal cutting and dies for drawing wire [3]; ZrC, because of its lower cost, is often added to TiC in these applications [4].

Several anodic dissolution studies have been performed on TiC and TiB_2. Cowling and Hintermann [5] and Fried and Lilin [6] have studied dissolution of TiC in sulphuric acid at voltages up to 2 V. Rambert *et al.* have investigated TiB_2 dissolution in aqueous NaCl, NaBr, $NaNO_3$ and HCl, and in two non-aqueous electrolytes: H_2SO_4 in methanol and $HClO_4$ in acetic acid. Applied voltages ranged from 0–50 V. They determined that electrochemical polishing was possible in several non-aqueous electrolytes whereas only rough surfaces were obtained after anodic dissolution in the aqueous solvents [7]. Anodic dissolution of TiB_2 and ZrB_2 in both aqueous and alcholic electrolytes was studied by

* *Present Address*: Department of Chemical Engineering, University of Florida, Gainesville, FL 32611, USA.

Abramov and Davydov [8]. They recommend aqueous chloride solutions for ECM of TiB_2 and ZrB_2.

As most refractory materials in their pure form are very brittle, binders such as cobalt or nickel are added to impart the toughness required for industrial applications. Petit *et al.* have studied the anodic dissolution of titanium–copper alloys at potentials up to $600\,mV\,s^{-1}$. Titanium was found to dissolve preferentially, leaving the surface of the alloy enriched with copper [9]. The ECM of several commercial titanium alloys has been investigated by Bannard, who observed that the two-phase alloys (IMI 550 and 685) exhibited preferential dissolution of one phase during machining [10, 11].

2. Experimental details

To make the experimental cuts, the cathode (toolpiece) was attached to a job shop gun drill (Hanson–Van Winkle–Munning) and advanced at a constant rate toward the anode (workpiece). At the same time, a voltage of 10–31 V was applied across the electrodes and an electrolyte solution was pumped between them at a high flow rate (1–10 litres min^{-1}). The experimental equipment used in this work has been described in detail elsewhere [12–14].

Two electrolytes were used: 2 M potassium nitrate and 3 M sodium chloride. The choice of NaCl was based on its widespread industrial use; KNO_3 is a more expensive electrolyte, but has been found to give a smoother surface finish in the ECM of many metals, including iron, copper, nickel, aluminium and cobalt [15]. The experimental set-up included an electrolyte recirculation system in which a series of three filters was used to remove the solid reaction products from the ECM effluent. The pure carbide and boride anodes investigated in this work were obtained from a commercial source [16], while the TiC/10% Ni specimens were fabricated on site, using standard cold-pressing and sintering techniques. Nickel samples were cut from a rod (Ni-200). Table 1 lists the composition and selected physical properties of each material investigated. Two types of cylindrical toolpiece were constructed for this study. One design provided a single hole in the electrode face for electrolyte flow; for the other type, five small holes were made in order to distribute the electrolyte more evenly. The electrode face was machined of brass or copper and the sides of the toolpiece were electrically insulated with KYNAR vinylidene fluoride resin. Toolpiece diameters ranged from 6 to 7 mm.

A series of runs involving a range of applied voltages (10–31 V) and toolpiece advancement rates (0.2–1.4 mm min^{-1}) was performed on each anode material. The pure carbides were machined in both KNO_3 and NaCl electrolytes, whereas the borides and the TiC/Ni composite and its component materials, TiC and Ni, were dissolved in 2 M KNO_3 only.

The independent operating variables that were set in this system were applied voltage, toolpiece advancement rate and electrolyte flow rate. Among the dependent variables measured were current, pressure and temperature of the electrolyte, and mass loss of the workpiece. Table 2 shows the ranges of values for some of the operating variables in this system, and for parameters derived from them. The appearance, composition and roughness of the anode surfaces were investigated by means of scanning electron microscopy (SEM), energy dispersive X-ray spectroscopy (EDXS), Auger electron spectroscopy (AES) and surfanalysis.

3. Results and discussion

3.1. *Carbides and borides*

3.1.1. Valence of dissolution. To determine the valence of dissolution, plots were made for each material using two forms of Faraday's Law,

$$\dot{m} = [(M/F)\,z]\,I \qquad (1)$$

$$\dot{x} = [(M/F)\,\varrho z]\,i \qquad (2)$$

Plotting $\dot{m}$ versus I and $\dot{x}$ versus i yielded straight lines with slopes related to z. For TiC, TiB_2 and ZrC the two values of z obtained matched each other within experimental error and z was found to be independent of current density. Fig. 1 shows a plot of $\dot{x}$ versus i for TiC; data from dissolution in each electrolyte fall on one line, the slope of which corresponds to a value of $z = 6.6$.

Table 1. Physical characteristics of anode materials

Material	*Hardness (Rockwell A)*	*Electrical conductivity* ($\Omega^{-1}cm^{-1}$)	*Density*		*Porosity (%)*	*Melting point (°C)*	*Formula weight* ($g\,gmol^{-1}$)	*Aspect and structure*	*Composition (wt %)*
			Observed ($g\,cm^{-3}$)	*Literature* ($g\,cm^{-3}$)					
TiC	96	1.18×10^{-4}	4.4	4.93	10.8	3150	59.911	Grey metallic, cubic	Ti: 80.0 C: 19.5 Fe, Si, Ca, Na, O, N, H: < 0.3
ZrC	92.5	1.54×10^{-4}	4.96	6.76	26	3530	103.23	Metallic, fcc	Zr: 88.4 C: 11.6
TiB_2	99	3.52×10^{-4}	4.43	4.50	1.5	2900	69.52	Grey, hexagonal	Ti: 68.30 B: 31.40 Fe, C, H, N, O: < 0.3
ZrB_2	87–89	10.8×10^{-4}	5.83	6.09	4.3	3040	112.84	Grey with cracks, hexagonal	Zr: 80.4 B: 19.15 Fe, C, O, N: < 0.35
TiC/Ni	—	—	4.8	5.42	11.4	—	59.8	Grey metallic, 2-phase	TiC: 77.2 C: 11.9 Ni: 9.7 Co: 1.2
Ni-200	40	15.6×10^{-4}	8.84	8.89	0.56	1453	58.71	Silver metallic, cubic	Ni: 99.4 C, Cu, Fe, Mn, S, Si: < 0.3
Cu	27	58.8×10^{-4}	—	8.94	—	1083	63.5	Red, fcc	Cu: 99.99 Impurities $\leqslant 0.01$

Table 2. Range of values for ECM operating variables and derived parameters

Parameter	*Symbol*	*Range of values*
Applied voltage	V	10–31 V
Toolpiece feed rate	$\dot{x}$	0.2–1.4 mm min^{-1}
Electrolyte flow rate	Q	1–10 litres min^{-1}
Electrolyte temperature	t	22–34° C
Current	I	8–42 A
Current density	i	14–116 A cm^{-2}
Mass removal rate	$\dot{m}$	0.05–0.5 g min^{-1}
Electrolyte conductivity	k	0.15–0.25 Ω^{-1} cm^{-1}
Interelectrode gap	l	0.25–1.32 mm

In the case of ZrB_2, however, z was found to decrease with increasing current density. An apparent valence of 9.8 eq mol^{-1} was obtained at high current densities, while 14 eq mol^{-1} was the valence observed at the lower end of the current density range investigated. This behaviour indicates a change in the dissolution chemistry of ZrB_2 with increasing current density. Table 3 lists the average valence values obtained for each anode material. Fig. 2 shows the individual values for valence plotted versus current density.

Anodic dissolution studies of TiC by Cowling and Hintermann yielded valence values ranging from 6.5 to 7.0 eq mol^{-1} [5]. Their results, obtained at much lower currents (0.01–0.6 mA cm^{-2}) and at correspondingly lower voltages (0.9–1.0 V), indicate a decrease of valence with increasing voltage.

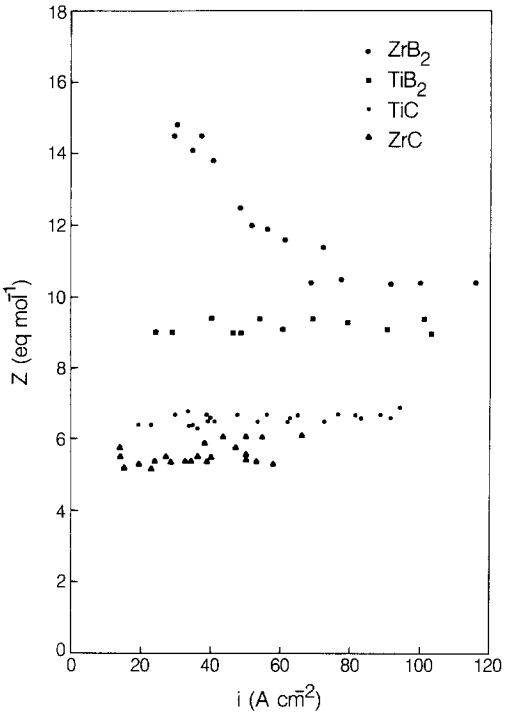

Fig. 2. Valence of dissolution versus current density for TiC and ZrC in KNO_3 and NaCl, and for TiB_2 and ZrB_2 in KNO_3.

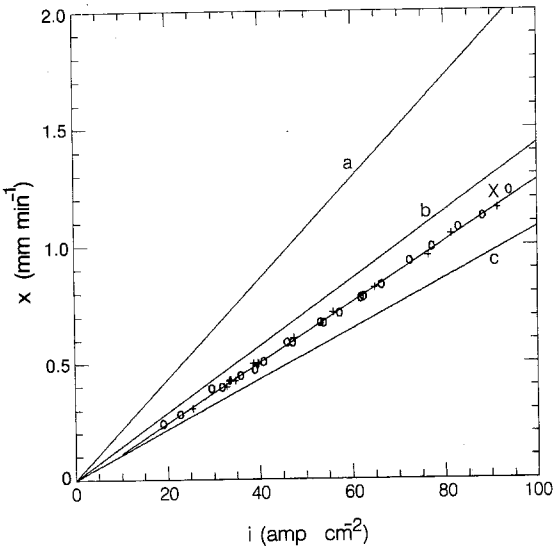

Fig. 1. Machining rate versus current density for TiC in 2 M KNO_3 (+) and 3 M NaCl (○). Line X: experimental correlation using both data sets. Theoretical lines: (a) 4 eq mol^{-1}; (b) 6 eq mol^{-1}; (c) 8 eq mol^{-1}.

3.1.2. Current–voltage relationship. Voltage versus current density plots were prepared for each anode material. Since the interelectrode gap could not be controlled during machining and was measured only after the termination of the experiment, the data for each material were grouped according to the resulting gap sizes. Then, for a given gap, voltage was plotted against current density. Fig. 3 shows two lines for the dissolution of TiC: one in KNO_3 at a gap of 0.30 mm and the other in NaCl at a gap of 0.58 mm. Straight-line current–voltage curves were also obtained for ZrC and TiB_2, but the curves for ZrB_2 exhibited a steeper slope at lower current densities, suggesting a different dissolution stoichiometry in this region.

Included in Fig. 3 are lines representing the ohmic drop across the electrolyte at the two gaps

Table 3. Carbides and borides: average valence of dissolution (z) *and IR-free cell voltage* ($V - V_{IR}$)

Material	z *(eq mol^{-1})*	*Range of* i *(A cm^{-2})*	*Range of* ($V - V_{IR}$) *(V)*
TiC	6.6	23–88	3–6
ZrC	5.7	19–81	3–11
TiB_2	9.3	15–103	5–8
ZrB_2	9.8	27–106	4–10

specified. For each electrolyte, the current–voltage curve lies above and roughly parallel to the ohmic drop line. This voltage difference is the *IR*-free cell voltage and is equal to the sum of the thermodynamic equilibrium potential and the overvoltages:

$$V - V_{IR} = E_0 + \Sigma\eta_i \qquad (3)$$

The ($V - V_{IR}$) values observed for TiC range from 3 to 6 V. Similar plots for the other anode materials yielded values ranging even higher, i.e. up to 11 V for ZrC. These ranges are listed in Table 3 along with the corresponding current density ranges.

One would expect the overvoltages in the equation above, and therefore ($V - V_{IR}$), to increase with current density. The current–voltage lines for ZrC do exhibit this behaviour, but most of the curves for the other anode materials are essentially parallel to the corresponding ohmic drop lines. In some cases the lines are not parallel. Because of the experimental uncertainties, it is difficult to claim any particular trends in dependence of ($V - V_{IR}$) on *i*. Estimated ranges of ($V - V_{IR}$) for carbides and borides of titanium and zirconium are given in Table 3. Apart from the ohmic drop across the interelectrode gap the cell voltage does not appear to demonstrate any dependence on current. In view of the large ohmic drop (17 and 26 V at 100 A cm^{-2} for the two solutions) and the relatively small current-dependent component expected from Tafel-type overpotential behaviour, our determination of interelectrode gap may not have been reliable enough to allow a precise assignment of voltage components. It is worth noting that a large, current-independent surface overpotential has been observed in the high-rate transpassive dissolution of copper [17, 18].

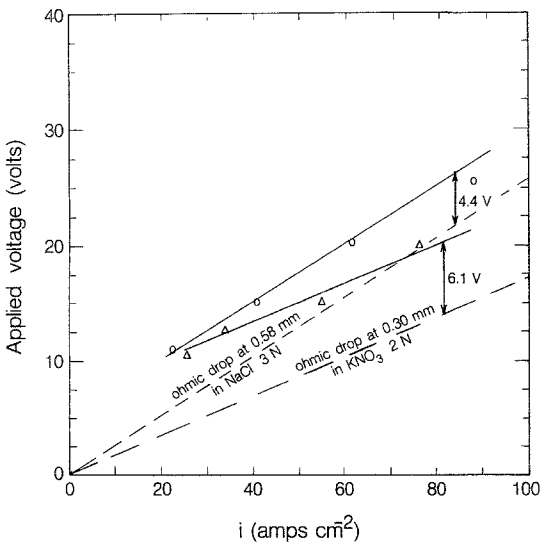

Fig. 3. Applied voltage versus current density for TiC in 2 M KNO_3 (Δ) at a gap of 0.58 mm and in 3 M NaCl (○) at a gap of 0.30 mm.

Kinoshita *et al.* [17] observed a transition from active to transpassive dissolution of copper accompanied by the formation of solid dissolution products consisting primarily of cuprous oxide. Landolt *et al.* [18] observed that the transition from active to transpassive dissolution, evidenced by a sharp increase in anode potential, was accompanied by the formation of a thin, well-adhering, solid layer on a copper anode. A large fraction of the cell voltage increase was found to be non-ohmic. Cooper *et al.* [19] described potential oscillations caused by the periodic formation and breakdown of surface layers.

3.1.3. Surface roughness and appearance. Surface roughness measurements were taken with a model 21 Skidless surfanalyser system (Clevite Corporation). The roughness of post-ECM surfaces of TiC and ZrC ranged from 3 to 10 μm. Roughness was found to be independent of

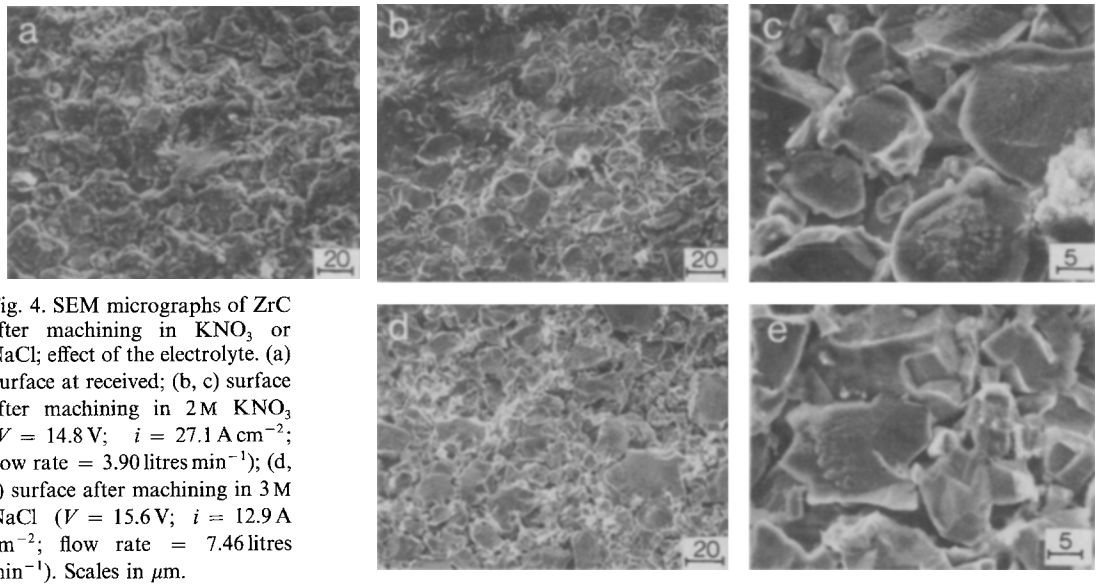

Fig. 4. SEM micrographs of ZrC after machining in KNO_3 or NaCl; effect of the electrolyte. (a) Surface at received; (b, c) surface after machining in 2 M KNO_3 (V = 14.8 V; i = 27.1 A cm^{-2}; flow rate = 3.90 litres min^{-1}); (d, e) surface after machining in 3 M NaCl (V = 15.6 V; i = 12.9 A cm^{-2}; flow rate = 7.46 litres min^{-1}). Scales in μm.

current density and electrolyte flow rate, but it varied with the electrolyte. A surface roughness of 5–6 μm was obtained for ZrC machined in 2 M KNO_3, while in 3 M NaCl the roughness ranged from 8 to 10 μm. This is to be compared with an original surface roughness of about 10 μm. While the roughness varied with electrolyte, the surface appearance of the post-ECM ZrC anodes was not noticeably affected (Fig. 4).

The surface appearance of the anode materials was examined by means of SEM. Surface brightening was not observed on any of the materials for the range of ECM operating conditions employed. For the carbides, the post-ECM surfaces looked very similar to the original surfaces (Fig. 5), whereas the borides exhibited a more etched appearance after machining (Fig. 6).

The effect of current density on surface appearance was found to be negligible for TiC, ZrC and TiB_2. Fig. 5 shows a series of SEM micrographs for TiC surfaces machined in KNO_3 at different current densities. The surface appearance of ZrB_2, however, varied with current density; an increasing coverage by a white

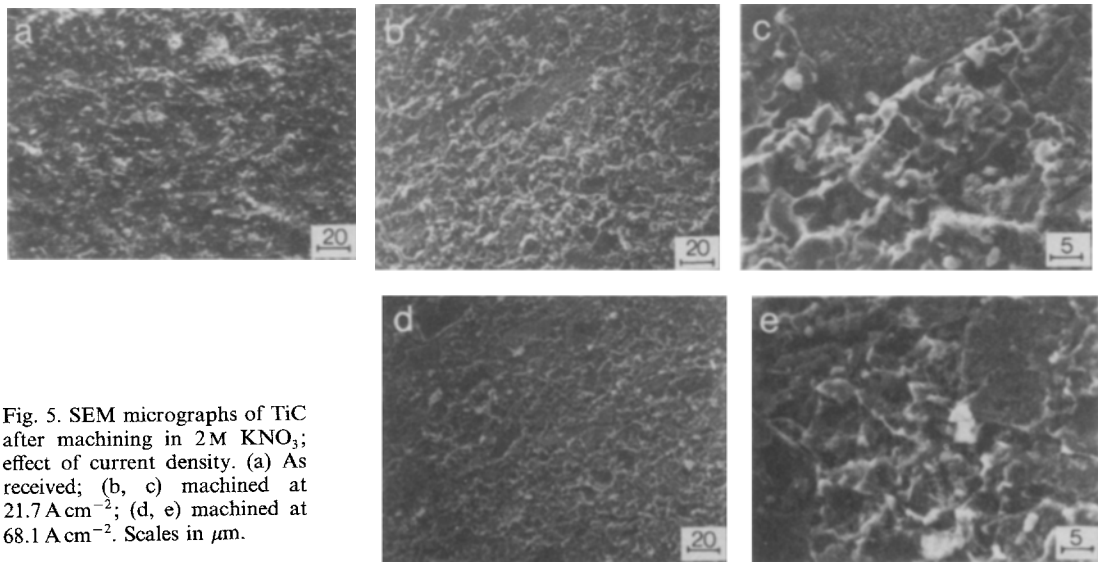

Fig. 5. SEM micrographs of TiC after machining in 2 M KNO_3; effect of current density. (a) As received; (b, c) machined at 21.7 A cm^{-2}; (d, e) machined at 68.1 A cm^{-2}. Scales in μm.

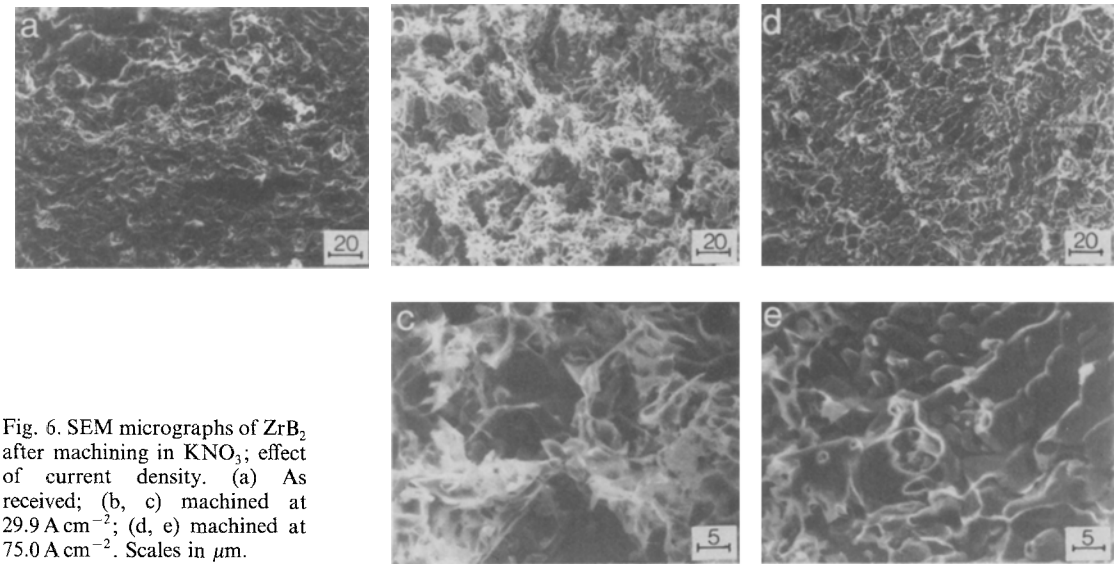

Fig. 6. SEM micrographs of ZrB_2 after machining in KNO_3; effect of current density. (a) As received; (b, c) machined at 29.9 A cm^{-2}; (d, e) machined at 75.0 A cm^{-2}. Scales in μm.

substance, possibly an oxide film, was observed with decreasing current density (Fig. 6). A greater coverage by such an oxide film would increase the relative rate of a side reaction, such as oxygen evolution; this could be responsible for the higher apparent valence of dissolution observed for ZrC at lower current densities.

3.1.4. Analysis of solid reaction products. Chemical analysis of the dissolved reaction products was not attempted in this work because of the very low concentrations of these species in the electrolyte (below 2 p.p.m.). In the case of TiC and TiB_2, however, solid reaction products in the form of a white powder were found on the walls of the ECM holes. This white powder was recovered and analysed by X-ray diffraction. Lines for titanium dioxide were observed in the diffraction patterns for both the TiC and the TiB_2 residual powders. In addition, lines for the ECM electrolytes, NaCl and KNO_3, were present. Diffraction lines were not observed for any of the other oxides of titanium, i.e. TiO, Ti_2O_3 and Ti_3O_4, nor for the titanates $NaTiO_2$ and $Na_2TiO_4H_2O$. Thus, for both TiC and TiB_2, the titanium appears to be oxidized only to the +4 state.

Although the reaction mechanism cannot be derived from the present work, the following overall reactions are proposed for the anodic dissolution of TiC and TiB_2 during ECM:

For TiC

$$TiC + 3H_2O \longrightarrow TiO_2 + CO + 6H^+ + 6e \qquad E_0 = +0.232\,V \tag{4}$$

and

$$TiC + 4H_2O \longrightarrow TiO_2 + CO_2 + 8H^+ + 8e \qquad E_0 = +2.66\,V \tag{5}$$

For TiB_2

$$TiB_2 + 8H_2O \longrightarrow TiO_2 + 2H_3BO_3 + 10H^+ + 10e \qquad E_0 = +0.593\,V \tag{6}$$

These reactions are based on the experimentally determined valences of dissolution and on the reaction product TiO_2 detected by X-ray diffraction. Similar results have been obtained by Cowling and Hintermann [5], who found that the anodic oxidation of TiC in 2 N H_2SO_4 yields Ti(IV) and both CO and CO_2.

3.2. *Cemented TiC/10% Ni*

3.2.1. ECM behaviour. The ECM behaviour of a TiC/10% Ni composite was investigated along with that of its component materials, TiC and Ni. Values for the valence of dissolution were obtained in the manner described above; the average values for the three materials are

Table 4. Cemented TiC/10% Ni and components: average valence of dissolution (z) *and IR-free cell voltage* ($V - V_{IR}$)

Material	z *(eq mol^{-1})*	($V - V_{IR}$) *(V)*
TiC	6.6	4.2
TiC/Ni	6.5	3.0
Ni-200	2.8	0.7

compared in Table 4. TiC/10% Ni dissolves with an apparent valence of 6.5. This is somewhat higher than the value of 6.2 which is the weighted average, 90 : 10, of the valences obtained for TiC and Ni when dissolved independently. The value of 2.8 obtained for the valence of dissolution of Ni-200 is higher than the value of 2.0 proposed by Datta and Landolt [20] and by MacDougall [21], who studied the anodic dissolution of nickel. This suggests that the current efficiency for nickel dissolution in this study is less than 100%, probably due to concurrent oxygen evolution. Since oxygen evolution could not be monitored in the system used in this study it was not possible to check the current efficiency of nickel dissolution independently. A current efficiency below 100% would result in higher valences for the reactions of TiC and TiC/Ni than the apparent valences given here.

All three materials exhibited linear dependence of current density on voltage. For TiC and TiC/Ni, the current–voltage curves were essentially parallel to the ohmic drop lines. In the case of nickel, the lines were convergent; however, the large experimental uncertainty for ($V - V_{IR}$) could be responsible for this convergence. The average values obtained for ($V - V_{IR}$) are listed in Table 4. Again, TiC/Ni exhibits a value intermediate to those obtained for TiC and Ni-200.

3.2.2. Surface analysis. The surface appearance of the TiC, TiC/Ni and Ni anodes was examined by means of SEM. Micrographs of typical post-ECM surfaces are shown in Fig. 7. In the case of TiC the appearance of the surface before and after machining is not significantly different. For both TiC/Ni and Ni, however, two phases are observed on the post-ECM surfaces. As shown in Fig. 7b and c, a delicately structured, white material appears to be partially covering a dark, chunky phase underneath. The white substances occurring on the TiC/Ni and Ni surfaces appear to be oxides.

For TiC and Ni-200, the post-ECM surfaces obtained at different machining conditions did not exhibit much variation. In the case of TiC/Ni, however, post-ECM surfaces obtained at low ECM rates exhibited regions of macro-roughness. This phenomenon became less prevalent on the machined surface at higher values of voltage and toolpiece feed rate. A polished surface was not obtained for TiC/10% Ni over the range of operating conditions investigated.

Surface compositions of the anodes were determined by means of EDXS and AES. Table 5 shows the EDXS results for TiC/Ni. The nominal 10 wt % composition of the original

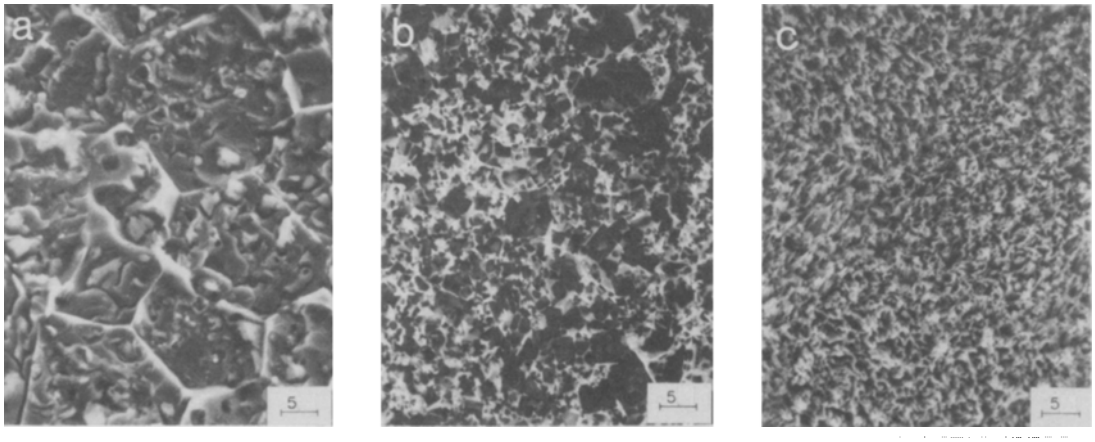

Fig. 7. SEM micrographs of typical post-ECM anode surfaces: (a) TiC; (b) TiC/Ni; (c) Ni-200. Machining conditions: $V = 15$ V; $\dot{x} = 0.5$ mm min^{-1}. Scales in μm.

*Table 5. Nickel content of post-ECM TiC/Ni surfaces, as obtained by EDXS analysis**

ECM operating conditions		*Smooth surface*		*Rough surface*	
Applied voltage (V)	$\dot{x}$ *(mm min^{-1})*	*Type*	*Nickel (%)*	*Type*	*Nickel (%)*
Before ECM	–	–	12	–	–
10	0.24	(S)	31	R	20
15	0.34	(S)	†	R	†
15	0.50	S	31	–	–
20	0.51	(S)	45	R	12
20	0.72	S	39	(R)	†
24	0.66	S	39	(R)	23
24	0.76	S	20	–	–
24	0.84	S	28	–	–
24	1.09	S	23	–	–

* The symbols for the surface types signify the following: S, smooth surface, predominant; (S), smooth surface, small region; R, rough surface, predominant; (R), rough surface, small region.
† Data not available.

material shows up as 11 wt % by EDXS analysis. The post-ECM compositions all show an increased nickel content and the smooth surface regions consistently exhibit higher values than the rough surfaces.

AES composition profiles taken on post-ECM TiC/Ni surfaces support the EDXS results. Fig. 8 shows a profile for a run at intermediate machining conditions ($V = 15$ V; $\dot{x} = 0.5$ mm min^{-1}). The major elemental components (titanium, nickel, carbon and oxygen) are traced over a total sputtering time of 20 min; this corresponds to about 0.4 μm of material removed. At the end of this time the profile of each element has begun to flatten out, indicating that the bulk composition of the TiC/Ni specimen has been reached.

Table 6 lists the initial and final amounts of each element shown in the profile. The concentrations of nickel and oxygen are high at the surface and decrease toward the bulk material,

Table 6. Surface and bulk compositions of post-ECM TiC/Ni obtained by AES

Element	*Surface composition (at %)*	*Bulk composition (at %)*
Nickel	47	11
Titanium	22	44
Carbon	10	39
Oxygen	21	6

whereas titanium and carbon increase into the bulk. The initial value of 47 at % for nickel is higher than that obtained by EDXS (31 at %), but both values are higher than that in the bulk (11 at %). Note that the error associated with the AES analysis is ± 5 at % or more, since the surfaces being examined are rougher than those usually studied by AES and since sensitivity factors for quantitative analysis of this matrix are uncertain. The amounts of titanium and carbon in the TiC/Ni surface are low, but they rise gradually to 44 at % and 39 at %, respectively, at a depth of about 0.4 μm. These values are not only close to each other, but also close to the expected value of 45 at % for both elements.

The behaviour of oxygen in the AES composition profile supports the presence of an oxide layer on the post-ECM surface, as suggested in the SEM micrographs. In the profile, the amount of oxygen detected at the surface is substantial, i.e. 21 at %; the thickness of the proposed oxide layer, however, is probably much less than suggested in the profile. Due to the roughness of the surface, the argon ion beam which strikes the surface at an angle is not able to sputter away the material evenly. Therefore, the analysing beam which is normal to the surface continues to detect any oxide that has been sheltered from the sputtering beam. The probable thickness of the oxide layer is something less than 40 nm. Eventually, the amount of oxygen drops off to 6 at % in the bulk; this value

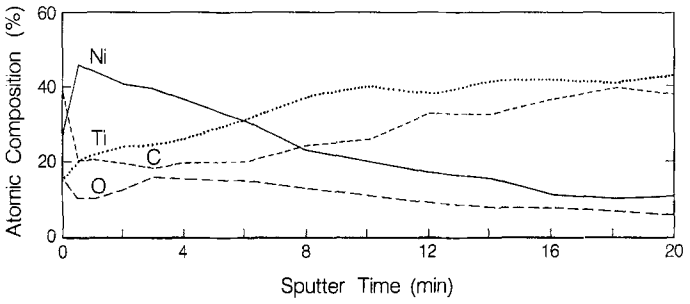

Fig. 8. AES composition profile of post-ECM TiC/Ni surface. Machining conditions: $V = 15\,\text{V}$; $\dot{x} = 0.5\,\text{mm min}^{-1}$.

is essentially negligible since it is very close to the ± 5 at % error limit.

The post-ECM TiC/Ni surfaces were examined further to determine the nature of the two phases, light and dark, that were observed in the SEM micrographs. EDXS and AES were once again employed. Fig. 9b shows an SEM micrograph of a post-ECM surface taken at high magnification ($\times 5000$). Light and dark regions are clearly distinguishable. To the left of the micrograph is an X-ray map for titanium (Fig. 9a), and to the right is a map for nickel (Fig. 9c). This set of pictures shows qualitatively, but clearly, that the light regions are generally rich in nickel while the dark regions are generally rich in titanium. Quantitative results were obtained by focusing on individual light and dark areas and determining their compositions from EDXS spectra. Table 7 summarizes the results for several smooth post-ECM surfaces. The nickel content of the light regions averages 49 at %, which is much higher than the average surface value (28 at %). In contrast, the dark regions appear to contain an average of only 19 at % nickel.

Spectra of light and dark regions on TiC/Ni were also obtained by AES. A spectrum for a light region is shown in Fig. 10. One observes fairly large signals for nickel and oxygen and moderate signals for titanium and carbon. In comparison, the spectrum for the dark region (Fig. 11) shows a smaller oxygen signal and only a minimal signal for nickel. These results correlate very well with the other evidence that indicates that the light phase is an oxide layer, and they suggest that the oxide is one of nickel.

Anodic oxide films have been observed on nickel by a number of authors [21, 22]. In particular, Datta *et al.* have detected very thin oxide layers formed on nickel surfaces during high-rate transpassive dissolution [22].

4. Conclusions

1. ECM has been shown to be a feasible method for machining both pure and cemented refractory

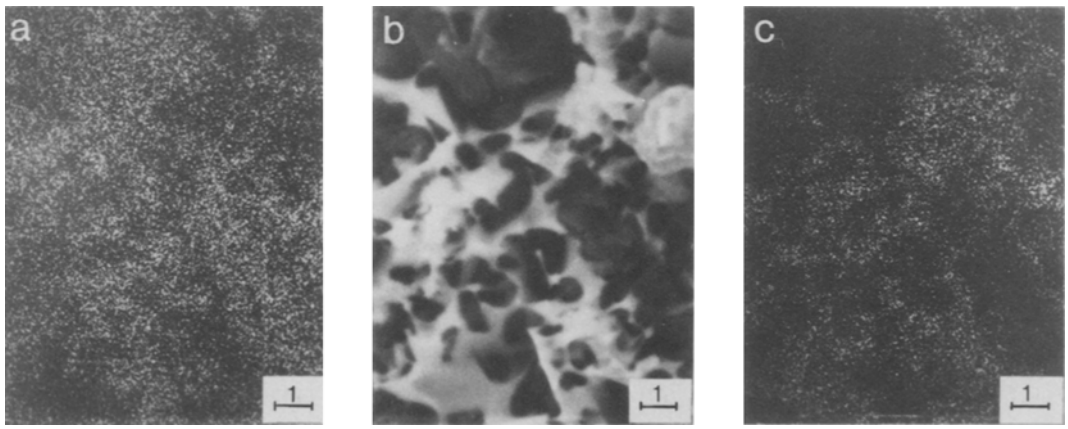

Fig. 9. Composition of post-ECM TiC/Ni surface. Machining conditions: $V = 15\,\text{V}$; $\dot{x} = 0.5\,\text{mm min}^{-1}$. (a) X-ray map for titanium, corresponding to (b). (b) SEM micrograph. (c) X-ray map for nickel, corresponding to (b). Scales in μm.

Table 7. Nickel content of different regions on smooth, post-ECM TiC/Ni surfaces as determined by EDXS (atomic composition, %)

Run	*Average surface (% Ni)*	*Light region*	*Dark region*
55	23	33	19
71	20	61	19
59	17	37	7
67	39	52	23
70	39	64	25
Average	28 ± 9	49 ± 12	19 ± 5

materials, i.e. TiC, ZrC, TiB_2, ZrB_2 and a cemented TiC/10% Ni composite.

2. For TiC, ZrC and TiB_2, the apparent valences of dissolution were found to be constant over the range of current densities investigated. In addition, a linear dependence of current density on cell voltage was observed for all three materials. The electrochemical behaviour of ZrB_2 was different: the apparent valence decreased with increasing current density, and the dependence of current density on voltage was not linear.

3. The post-ECM surface roughness of TiC and ZrC ranged from 3 to 10 μm and was found to be dependent only on the type of electrolyte used during machining.

4. The ECM behaviour of TiC/10% Ni is intermediate to that of its pure components, TiC and nickel.

5. The TiC phase dissolves preferentially to the nickel phase during ECM of the composite over the entire range of operating conditions investigated.

6. The presence of a thin oxide layer is suggested on the post-ECM surfaces of TiC/Ni and Ni.

7. In the current density range employed in this study, TiC/10% Ni does not develop a polished surface after ECM in 2 M KNO_3.

Acknowledgements

This work was supported by the Director of the Office of Energy Research, Office of Basic Energy Sciences, Materials Sciences Division of the US Department of Energy under Contract No. DE-AC03-76SF00098. We also wish to thank Mr Kenneth Gaugler for his assistance with the scanning electron micrographs and the Auger analysis.

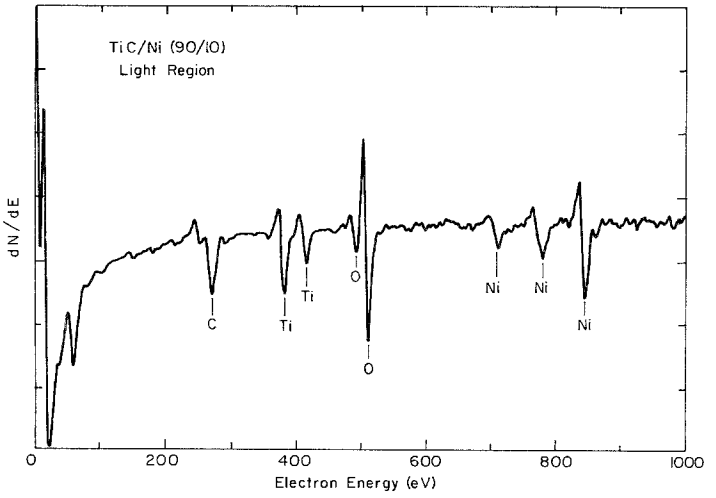

Fig. 10. AES spectrum of light-coloured region on post-ECM TiC/Ni surface. Machining conditions: $V = 15$ V; $\dot{x} = 0.5$ mm min^{-1}.

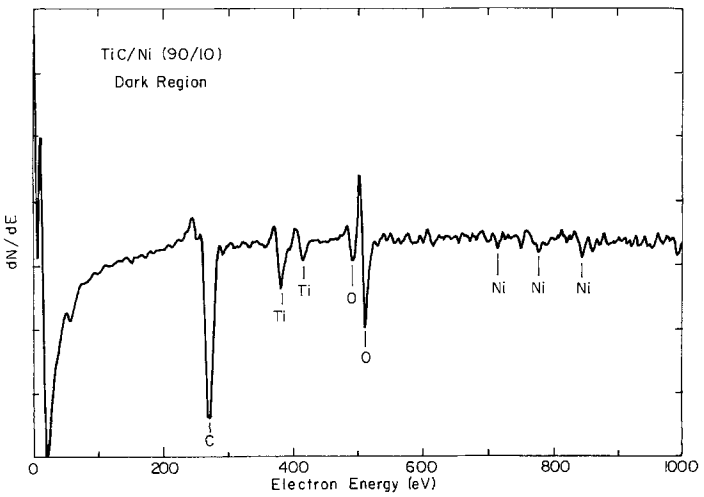

Fig. 11. AES spectrum of dark-coloured region on post-ECM TiC/Ni surface. Machining conditions: $V = 15\,V$; $\dot{x} = 0.5\,mm\,min^{-1}$.

References

[1] 'Engineering Properties of Selected Ceramic Materials' (edited by J. F. Lynch, C. G. Ruderer and W. H. Duckworth), American Ceramic Society, Columbus, Ohio (1966).

[2] 'Refractory Ceramics for Aerospace: A Materials Selection Handbook' (edited by J. R. Hague *et al.*), American Ceramic Society, Columbus, Ohio (1964).

[3] R. L. Sands and C. R. Shakespeare, 'Powder Metallurgy: Practice and Applications', William Clowes, London (1966).

[4] P. Schwarzkopf and R. Kieffer, 'Refractory Hard Metals: Borides, Carbides, Nitrides and Silicides', MacMillan, New York (1953).

[5] R. D. Cowling and H. E. Hintermann, *J. Electrochem. Soc.* **118** (1971) 1912.

[6] M. Kh. Freid and S. A. Lilin, *Sov. Electrochem.* **15** (1979) 137.

[7] S. Rambert, R. Sautebin and D. Landolt, *Oberflaeche-Surface* **22** (1981) 46.

[8] Yu. A. Abramov and A. D. Davydov, *Sov. Electrochem.* **16** (1980) 342.

[9] J. A. Petit, P. Lafargue, L. Porte and Tran Minh Duc, *Electrochim. Acta* **24** (1979) 1023.

[10] J. Bannard, *J. Appl. Electrochem.* **6** (1976) 477.

[11] *Idem, ibid.* **4** (1974) 229.

[12] J. B. Riggs, R. H. Muller and C. W. Tobias, *Electrochim. Acta* **26** (1981) 961.

[13] B. A. Dissaux, MS Thesis, University of California, Berkeley, 1978. (LBL-8023).

[14] C. A. Coughanowr, MS Thesis, University of California, Berkeley, 1982. (LBL-13682).

[15] J. F. Wilson, 'Practices and Theory of Electrochemical Machining', Wiley, New York (1971).

[16] Haselden Company, San Jose, California.

[17] K. Kinoshita, D. Landolt, R. H. Muller and C. W. Tobias, *J. Electrochem. Soc.* **117** (1970) 1246.

[18] D. Landolt, R. H. Muller and C. W. Tobias, *ibid.* **118** (1971) 40.

[19] J. F. Cooper, R. H. Muller and C. W. Tobias, *ibid.* **127** (1980) 1733.

[20] M. Datta and D. Landolt, *Electrochim. Acta* **25** (1980) 1263.

[21] B. MacDougall, *J. Electrochem. Soc.* **127** (1980) 789.

[22] M. Datta, H. J. Matthieu and D. Landolt, *Electrochim. Acta* **24** (1979) 843.